UC Irvine
Faculty Publications

Title

Global climatology of abundance and solar absorption of oxygen collision complexes

Permalink

https://escholarship.org/uc/item/08v3z6fw

Journal

Journal of Geophysical Research, 104(D20)

ISSN

Author

Zender, Charles S.

Publication Date

1999-10-01

DOI

Copyright Information

Peer reviewed

Global climatology of abundance and solar absorption of oxygen collision complexes

Charles S. Zender[1]

National Center for Atmospheric Research, Boulder, Colorado

Abstract. To improve our understanding of the absorption of solar radiation in the atmosphere we have characterized the spectral absorption, the spatial and temporal abundance, and the radiative forcing of the oxygen collision pairs $O_2 \cdot O_2$ and $O_2 \cdot N_2$ ($O_2 \cdot X \equiv O_2 \cdot O_2 + O_2 \cdot N_2$). The regional, vertical, seasonal, and annual patterns of $O_2 \cdot X$ abundance and radiative forcing are obtained from a general circulation model. We estimate the mean absorption by $O_2 \cdot X$, heretofore neglected in large scale atmospheric models, is 0.75–1.2 W m^{-2}, or 1–2% of total atmospheric solar absorption. $O_2 \cdot X$ absorption reduces surface insolation by 0.48–0.78 W m^{-2} and increases the net radiative flux at the tropopause by 0.32–0.52 W m^{-2}. These ranges bracket the uncertainties due to spectral absorption cross sections, $O_2 \cdot N_2$ efficiency, $O_2 \cdot X$ abundance, and cloud distribution. Globally averaged, $O_2 \cdot X$ enhances absorption equally in clear and in cloudy skies.

We create a global climatology of well-mixed collision complex abundances by scaling $O_2 \cdot X$ abundance to other complexes such as $N_2 \cdot N_2$ and $O_2 \cdot Ar$. Collision complex abundance depends quadratically on the concentrations of the constituents. This dependence causes a 20% increase in $O_2 \cdot X$ abundance in the Arctic relative to the Tropics for the same sea level pressure. The variations in zonal mean $O_2 \cdot X$ abundance due to surface elevation, the annual mean meridional temperature gradient, and to seasonal temperature variations are 40, 15, and 10%, respectively. $O_2 \cdot X$ heating obeys the weakly absorbing, linear limit so it peaks at the surface in clear skies, but clouds shift this peak up by 200–300 mb on seasonal timescales. Surface albedo and clouds strongly modulate the solar forcing efficiency of $O_2 \cdot X$ (forcing per unit abundance) by altering the mean photon path length. These factors produce annual mean forcing maxima in the subtropics over bright deserts and regions of marine stratus. Inclusion of $O_2 \cdot X$ in models is likely to reduce cold biases in the summertime polar atmosphere, where $O_2 \cdot X$ contributes 2–4% of total solar heating.

1. Introduction

Our ability to balance the solar radiation budget of the atmosphere is uncertain [e.g., *Stephens and Tsay*, 1990; *Kato et al.*, 1997; *Ramanathan and Vogelmann*, 1997; *Collins*, 1998, and references therein]. Until we can perform this fundamental task, our skill at predicting the all sky radiation budget, and hence at predicting climate and climate change, will continue to be highly uncertain [e.g., *Cess et al.*, 1989]. The atmospheric collision complexes of oxygen $O_2 \cdot O_2$ and $O_2 \cdot N_2$ (henceforth $O_2 \cdot X \equiv O_2 \cdot O_2 + O_2 \cdot N_2$) have recently been identified as contributors to discrepancies between modeled and observed surface insolation [*Pfeilsticker et al.*, 1997; *Solomon et al.*, 1998]. $O_2 \cdot X$ presents a timely and interesting case for a radiative budget study because its solar absorption cross section is relatively well known, but its

abundance and absorption have not been characterized at the global scale necessary to fully describe its impact on climate.

The absorption features of oxygen collision complexes have been studied in the laboratory and in the atmosphere for many decades [*Perner and Platt*, 1980; *Solomon et al.*, 1998, and references therein]. Collisions relax the selection rules for dipole-forbidden transitions in one or both O_2 molecules, allowing for absorption during the collision. The detection of discrepancies between modeled and observed solar radiation in cloudy skies [*Cess et al.*, 1995; *Ramanathan and Vogelmann*, 1997] provoked interest in whether $O_2 \cdot X$ contributes to this discrepancy [*Erle et al.*, 1995; *Murcray et al.*, 1997] and in what its global radiative forcing characteristics are.

Pfeilsticker et al. [1997] first estimated the global annual mean solar absorption by $O_2 \cdot O_2$ in clear sky and in all sky (i.e., including clouds) conditions as 0.53 and 0.57 W m^{-2}, respectively. Two newer estimates include the effects of the powerful 1.27 μm band and of nitrogen induced absorption ($O_2 \cdot N_2$) in this band. Estimates from these studies suggest that globally and annually averaged, $O_2 \cdot X$ absorbs 0.9–1.3 W m^{-2} [*Solomon et al.*, 1998] or 0.84 W m^{-2} [*Mlawer et al.*, 1998]. Thus $O_2 \cdot X$ is thought to contribute 1–

[1]Now at Department of Earth System Science, University of California at Irvine.

2% of the total solar atmospheric absorption of 67 W m^{-2} (out of 342 W m^{-2} incoming) [Kiehl and Trenberth, 1997]. These estimates of $O_2 \cdot X$ absorption are based on single column line-by-line, multiple-scattering radiative transfer models which have been extensively validated against atmospheric observations by high spectral resolution instruments. The disparity in the latter two estimates is mostly due to uncertainties in absorption cross sections for $O_2 \cdot X$ bands in the near infrared and, to a lesser extent, from extrapolating single-column results to global annual means.

We use the term "radiative forcing" to denote various measures of the influence of atmospheric heating by $O_2 \cdot X$ on the climate system. Line-by-line estimates of $O_2 \cdot X$ absorption are too computationally expensive to convey the rich regional and seasonal behavior of $O_2 \cdot X$ radiative forcing caused by variations in temperature, pressure, elevation, clouds, surface albedo, and mixing ratios of other radiatively active atmospheric constituents. A general circulation model (GCM) is best suited to provide self-consistent, time-varying realistic distributions of $O_2 \cdot X$ forcing. Employing a GCM allows us to extend prior studies and to provide additional forcing metrics, including clear versus cloudy sky forcing, surface forcing, and net forcing at the tropopause. These metrics allow us to compare the radiative forcing by $O_2 \cdot X$ to other absorbers, including greenhouse gases. These comparisons, in turn, help to prioritize implementation of $O_2 \cdot X$ physics in large-scale atmospheric models. It is worthwhile noting that in contrast to anthropogenically influenced greenhouse gas concentrations, $O_2 \cdot X$ abundance is not changing.

To our knowledge no prior study has constructed a systematic global climatology for any collision complex (or dimer). Moreover, the regional, seasonal, and vertical patterns of $O_2 \cdot X$ abundance generalize to all complexes formed from well-mixed gases. Thus these patterns, which depend mainly on the meridional temperature gradient and orographic features, apply to all well-mixed collision complexes, for example, $N_2 \cdot N_2$, $O_2 \cdot Ar$, and $O_2 \cdot CO_2$. The patterns of $O_2 \cdot X$ radiative forcing, which depend additionally on insolation, surface albedo, and cloud cover, only apply to other complexes with absorption features similar to those of $O_2 \cdot X$. Thus, by characterizing $O_2 \cdot X$ abundance and forcing, we automatically obtain insight into all well-mixed collision complexes.

Establishing the spatial and temporal patterns of $O_2 \cdot X$ abundance and forcing will also help future studies ascertain whether unexplained atmospheric solar absorption is consistent with absorption by collision complexes (or dimers) of well-mixed molecules. The existence of complexes besides $O_2 \cdot X$ which cause significant solar radiative forcing is highly speculative. All significant structured atmospheric absorption measured in the atmosphere for large portions of the solar spectrum has been convincingly attributed to known absorbers [Pfeilsticker et al., 1997; Solomon et al., 1998; Mlawer et al., 1998; Vogelmann et al., 1998]. Moreover, a number of recent field studies explains all observed broadband clear sky solar absorption to within the uncertainties in the observations and models [Conant et al., 1997;

Zender et al., 1997; Ramanathan and Vogelmann, 1997; Jing and Cess, 1998]. However, Kato et al. [1997] and Halthore et al. [1998] find inexplicable discrepancies between models and observations of the clear sky diffuse field, and many independent studies show enhanced cloudy sky solar absorption relative to model predictions on both local and global scales [Cess et al., 1995; Zender et al., 1997; Collins, 1998]. Since $O_2 \cdot X$ has been proposed as a candidate for explaining some of these discrepancies [Erle et al., 1995; Murcray et al., 1997], this study attempts to bound the role of $O_2 \cdot X$ in explaining enhanced absorption in clear and cloudy skies.

The remainder of this study is organized as follows: Section 2 presents the nomenclature of collision complexes and summarizes the laboratory measurements of $O_2 \cdot X$ cross sections. Section 3 illustrates the modeled spectral characteristics of $O_2 \cdot X$ absorption during a field campaign and shows its net vertical heating signature in an idealized atmosphere. Section 4 presents the regional, seasonal, and vertical climatologies of $O_2 \cdot X$ abundance and forcing and generalizes $O_2 \cdot X$ abundance to other well-mixed collision complexes. Section 5 summarizes the results and discusses their implication for future studies of the atmosphere.

2. Characterization of Abundance and Absorption Cross Section

Quantifying the global radiative forcing of a gaseous molecular species i requires characterization of both its concentration $n_i(x, y, z, t)$ molecule cm^{-3} and its absorption cross section $\sigma_i(\lambda)$ cm^2 molecule^{-1}. The convolution of these two quantities with the instantaneous radiation field yields the instantaneous forcing due to the gas. However, careful laboratory measurements provide convincing evidence that for atmospheric temperatures and solar wavelengths, $O_2 \cdot X$ absorption is due to transient collision complexes rather than bound dimers (or van der Waals complexes) [Greenblatt et al., 1990; Orlando et al., 1991]. Since $O_2 \cdot X$ is not a bound molecule, we begin by defining properties analogous to n_i and σ_i, but that apply to collision complexes.

2.1. Abundance

The "abundance" $n_{X \cdot Y}$ of a collision complex of molecules X and Y is analogous to a traditional number concentration of a molecular species. We define $n_{O_2 \cdot X} \equiv n_{O_2} n_X$ where n_{O_2} and n_X are the number concentrations of O_2 and of its collision partner (N_2 or O_2, unless otherwise specified) in molecule cm^{-3}, respectively. Thus the dimensions of $n_{O_2 \cdot X}$ are molecule^2 cm^{-6}. By definition, $n_{O_2 \cdot X}$ is linearly proportional to the frequency of collisions of O_2 with X. To graphically depict the total column abundance of $O_2 \cdot X$, we will present the vertical column paths $N_{O_2 \cdot X}$ defined by

$$N_{O_2 \cdot O_2} \equiv \int_0^{TOA} n_{O_2 \cdot O_2} \, dz = \int_0^{TOA} n_{O_2}^2 \, dz$$

$$N_{O_2 \cdot N_2} \equiv \int_0^{TOA} n_{O_2} n_{N_2} \, dz = \gamma N_{O_2 \cdot O_2} \tag{1}$$

where the integration over z (height) is from the surface ($z = 0$) to the top of atmosphere (TOA $\approx$ 1.5 mb due to GCM vertical discretization). Likewise, the column path of a molecule X, in molecule cm^{-2}, will be denoted by N_X. We assume in (1) that the volume mixing ratios of N_2 and O_2 are constant in the Earth's atmosphere and that their ratio is the constant $\gamma \equiv n_{N_2}/n_{O_2} = 3.72787$ [*Goody and Yung*, 1989, p. 9]. Since the vertical profile of $n_{O_2 \cdot X}$ varies with the square of atmospheric density, variations in γ above the stratosphere have negligible impact on the column abundance, and thus forcing, of $O_2 \cdot X$.

2.2. Absorption Cross Sections

The absorption bands of the $O_2 \cdot O_2$ and $O_2 \cdot N_2$ collision complexes have been studied for decades. *Solomon et al.* [1998] give an excellent review of laboratory research on oxygen collision complex absorption. Here we summarize only the research necessary to understand the physical parameterizations and uncertainties present in this study.

Laboratory measurements of $O_2 \cdot X$ absorption infer a binary absorption coefficient $\sigma^b(\lambda)$ from the quadratic dependence of measured absorption on O_2 concentration, n_{O_2}. *Newnham and Ballard* [1998] provide a detailed description of this type of measurement and its uncertainties. The dimensions of $\sigma^b(\lambda)$ are cm^5 molecule^{-2}. Thus, for a given concentration n_{O_2} molecule cm^{-3} and path length Δz centimeters of collision partner (O_2 or N_2), the optical depths $\tau_{O_2 \cdot X}$ due to $O_2 \cdot X$ at wavelength λ are

$$\tau_{O_2 \cdot O_2}(\lambda) = \sigma^b_{O_2 \cdot O_2}(\lambda)\, n^2_{O_2} \Delta z \quad (2)$$

$$\tau_{O_2 \cdot N_2}(\lambda) = \sigma^b_{O_2 \cdot N_2}(\lambda)\, n_{O_2} n_{N_2} \Delta z$$

$$= \gamma\, \epsilon_{N_2} \sigma^b_{O_2 \cdot O_2}(\lambda)\, n^2_{O_2} \Delta z$$

$$\tau_{O_2 \cdot N_2}(\lambda) = \gamma\, \epsilon_{N_2} \tau_{O_2 \cdot O_2}(\lambda) \quad (3)$$

where (3) applies to the 1.27 μm band only (see Plate 1) and ϵ_{N_2}, discussed below, is the efficiency of N_2 (relative to O_2) at inducing O_2 absorption through collisional processes (i.e., $\sigma^b_{O_2 \cdot N_2} = \epsilon_{N_2} \sigma^b_{O_2 \cdot O_2}$).

Plate 1 shows the solar absorption continua for $O_2 \cdot X$ measured by *Greenblatt et al.* [1990] at ~ 0.15 nm resolution for $0.335 < \lambda < 1.137$ μm. The 1.27 μm band has not been adequately examined with modern laboratory techniques, so we adopt the cross sections for this band recommended by *Solomon et al.* [1998]. On the basis of a number of earlier measurements, Solomon et al. constructed the 1.27 μm band by stretching the measured 1.06 μm band to a full width at half maximum (FWHM) of 180 cm^{-1} and scaling its integrated band intensity by 1.6. The cross sections of O_3 and O_2 [*World Meteorological Organization*, 1985], and of NO_2 [*Davidson et al.*, 1988], are shown for comparison. The red curves show that significant $O_2 \cdot O_2$ solar absorption occurs in two spectral regions: $0.3 < \lambda < 0.7$ μm and $1.0 < \lambda < 1.4$ μm. $O_2 \cdot O_2$ visible absorption is due to simultaneous collision induced transitions in both O_2 molecules, while near-infrared absorption involves only one O_2 transition.

Newnham and Ballard [1998] recently measured $\sigma^b_{O_2 \cdot O_2}$ for $0.455 < \lambda < 0.830$ μm and compared their measure-

ments to those of *Greenblatt et al.* [1990] (Plate 1). The maximum $\sigma^b_{O_2 \cdot O_2}$ and the integrated band intensities of most bands differed by $< 20\%$ between the two sets of measurements. Greenblatt et al. found the integrated band intensity of the bands centered at 360, 380, and 477 nm varied by $< 15\%$ from $T = 296$ K to 196 K. Newnham and Ballard found the integrated band intensity of four bands from 532–630 nm varied by $< 10\%$ from $T = 283$ K to 223 K but that the intensity of the 477 nm band decreased by 30% over this temperature range. Thus the two studies disagree on the temperature dependence of the the only band examined in both studies, the 477 nm band. Why the disagreement at 477 nm exceeds the stated error bars of the two studies is unexplained. Balloon-borne observations of the 447, 532, and 577 nm bands by *Osterkamp et al.* [1998] recorded a 20% decrease in $\sigma^b_{O_2 \cdot O_2}$ as the temperature increased from $T = 200$ K to 300 K. Note that this decrease is in contrast to the increase of $\sigma^b_{O_2 \cdot O_2}$ with T measured by Newnham and Ballard in the 477 nm band. Osterkamp et al. conclude that $O_2 \cdot O_2$ may be a metastable complex with some dimer-like properties. For simplicity, our study assumes $\sigma^b_{O_2 \cdot X}$ is constant with temperature. However, we should remain open to the possibility that $\sigma^b_{O_2 \cdot X}$ varies significantly with temperature for some bands.

The parameter ϵ_{N_2} defines the efficiency of N_2 relative to O_2 as a partner for inducing absorption in the O_2 1.27 μm band. The upper and lower blue curves centered at $\lambda = 1.27$ μm in Plate 1 correspond to $\sigma^b_{O_2 \cdot N_2}$ assuming $\epsilon_{N_2} = 0.1$ and 0.3, respectively. All prior studies show $0.1 \leq \epsilon_{N_2} \leq 0.3$, and the preponderance suggest $\epsilon_{N_2} = 0.3$ (see discussion by *Solomon et al.* [1998]).

Solomon et al. [1998] used differential optical absorption spectroscopy at large zenith angles to show their high spectral resolution (≈ 0.6 nm) in situ measurements agree with the laboratory cross sections of *Greenblatt et al.* [1990] (Plate 1) to within 0.3% for the $O_2 \cdot O_2$ band at 0.63 μm. *Mlawer et al.* [1998] recently inferred $\sigma^b_{O_2 \cdot X}$ for $1.0 < \lambda < 1.57$ μm from field measurements with a high-resolution (0.6 cm^{-1}) interferometer. They inferred comparable peak intensities in the 1.06 and 1.27 μm $O_2 \cdot X$ bands, but narrower FWHMs, than previous investigators [*Solomon et al.*, 1998]. These narrower FWHMs would reduce absorption in the near-infrared $O_2 \cdot X$ bands by about 30% relative to Greenblatt et al. and Solomon et al.

The uncertainties in $\sigma^b_{O_2 \cdot X}(\lambda)$ contribute roughly half of the uncertainty in our estimate of global $O_2 \cdot X$ forcing. The uncertainty in $\sigma^b_{O_2 \cdot X}(\lambda)$ is $< 10\%$ for $0.335 < \lambda < 1.137$ μm [*Greenblatt et al.*, 1990]. Uncertainty in 1.27 μm band absorption is $\sim 30\%$. This was estimated by extrapolating to global scale the difference between single-column simulations employing the continua proposed by *Solomon et al.* [1998] and by *Mlawer et al.* [1998]. For consistency, our study adopts the same cross sections as Solomon et al., but we note two choices that keep our results for total $O_2 \cdot X$ absorption closer to those of Mlawer et al. First, we use $\epsilon_{N_2} = 0.2$, a somewhat conservative value. Second, we neglect the $O_2 \cdot O_2$ absorption band near 1.58 μm. This band absorbs $\sim 9\%$ as much as the 1.27 μm band [*Mlawer et al.*,

1998]. Appending the 1.58 μm continuum to the Solomon et al. cross sections would increase our computed total $O_2 \cdot X$ solar forcing by $\sim 4\%$. Other absorption features of $O_2 \cdot X$ are negligible in terms of the total absorbed solar irradiance. These features, and those of many other well-mixed collision complexes, are summarized in Table 1.

3. High Resolution Single Column Simulations

$O_2 \cdot X$ complexes are a relatively recent addition to the longstanding group of solar absorbers considered in large-scale atmospheric models: H_2O, O_3, O_2, NO_2, and CO_2. As such, the spectrally and vertically dependent features of $O_2 \cdot X$ absorption have not yet been thoroughly characterized in the literature. We now analyze these features in high-resolution, single-column simulations in order to better understand their implications on global-annual scales.

3.1. Spectral Characteristics and Overlap

Two previous studies characterized aspects of the spectral overlaps between $O_2 \cdot X$ and more familiar absorbers. *Pfeilsticker et al.* [1997, Figure 2] show $O_2 \cdot X$ spectral features at surface and TOA for $335 < \lambda < 1137$ nm. *Solomon et al.* [1998, Figure 2] show residual surface absorption spectra of $O_2 \cdot O_2$, O_2, and H_2O in the region $610 < \lambda < 680$ nm. To complement these studies, our Plate 2 shows the modeled absorption optical depth $\tau_{abs}(\lambda)$ of all significant gaseous solar absorbers for $200 < \lambda < 1400$ nm. The spectra represent local solar noontime (solar zenith angle $\theta = 45.128°$) for October 15, 1995, at the Clouds and Radiation Testbed (CART) site in Oklahoma. This was a pristine day with minimal aerosol burden ($0.04 < \tau_{0.5\mu}^{aer} < 0.05$, not shown), low precipitable water (11.6 kg m^{-2}), low column O_3 (233 DU), and estimated column NO_2 of 5×10^{19} m^{-2}. *Zender et al.* [1997] describe the multistream narrow band (10 cm^{-1}) Malkmus model, the experimental uncertainties, and all the input data in more detail.

Plate 2 isolates the solar absorption continuum (using $\sigma_{O_2 \cdot X}^b$ from Plate 1) of each gaseous absorber considered in the model. $O_2 \cdot X$ shares with H_2O the distinction of overlapping with all the significant solar absorbers. The strongest visible bands of $O_2 \cdot O_2$ overlap with the center of the O_3 Chappuis bands near 0.6 μm. The $O_2 \cdot O_2$ band at 0.630 μm overlaps the discrete O_2 γ band at 0.629 μm. The strong 1.06 μm band partially overlaps a saturated water vapor band, but its center is the strongest nonoverlapped feature of $O_2 \cdot O_2$ in the spectrum. Absorption at 1.27 μm shows strong overlap among the oxygen infrared band, $O_2 \cdot O_2$, and $O_2 \cdot N_2$. Although 1.27 μm is in a water vapor window, both wings of the $O_2 \cdot X$ bands centered there overlap with weak CO_2 bands and with the wings of H_2O bands. This overlap with H_2O lessens somewhat in dry air masses where column moisture is < 5 kg m^{-2} (e.g., Antarctica), but $O_2 \cdot X$ absorption is only weakly sensitive to variations in H_2O (see section 4.3). As Plate 2 shows, contributions of $O_2 \cdot N_2$ and $O_2 \cdot O_2$ to the total 1.27 μm continuum are nearly equal if $\epsilon_{N_2} = 0.2$. Using $\epsilon_{N_2} = 0.3$ (and weaker $\sigma_{O_2 \cdot X}^b(1.27 \mu m)$), *Mlawer et al.* [1998] found $O_2 \cdot N_2$ absorption may exceed $O_2 \cdot O_2$ absorption in this band by 15%.

The $O_2 \cdot O_2$ band at 0.477 μm occupies a relatively transparent spectral region where it is often stronger than any other gaseous absorber, i.e., O_3 or NO_2. This band is discernible in routine optical depth spectra taken at the CART site and other locations [*Michalsky et al.*, 1999]. Note that neglecting $O_2 \cdot O_2$ absorption in its stronger bands could bias operational retrievals of other absorber amounts (e.g., O_3, NO_2, or aerosol), leading to overestimates of order 0.01 optical depths. Fortunately, we are aware of no operational retrievals that are compromised by neglect of $O_2 \cdot O_2$ absorption. For this particular profile, we estimate $O_2 \cdot X$ causes 2.3 W m^{-2}, or 1.4%, of the total modeled atmospheric solar absorption of 164 W m^{-2}. Accounting for this absorption reduces the discrepancy between noontime modeled and observed surface insolation (773 and 760 W m^{-2}, respectively) from 13.0 to 11.2 W m^{-2} [*Zender et al.*, 1997].

3.2. Vertical Heating Profile

To illustrate the vertical profile of $O_2 \cdot X$ heating, we simulated "climatological" clear and cloudy sky, aerosol-free heating profiles for a 92 level midlatitude summer atmosphere [*Briegleb*, 1992]. Figure 1 shows the resulting vertical profile of total solar heating for the clear sky profile, the $O_2 \cdot X$ contribution to this clear sky heating, and the $O_2 \cdot X$ cloudy sky heating. The solar zenith angle ($\theta = 60°$), surface albedo ($A = 0.2$), and cloud properties (100 mb thick liquid stratus cloud centered at 850 mb, condensate path 100 g m^{-2}) represent climatological atmospheric properties. The $O_2 \cdot X$ heating profiles are multiplied by a factor of 100 for clarity.

The clear sky $O_2 \cdot X$ heating increases rapidly with pressure, peaking at the surface. Thus $O_2 \cdot X$ clear sky heating weakly destabilizes the atmospheric column. At moderate zenith angles, $O_2 \cdot X$ absorption is relatively weak (i.e., $\tau_{O_2 \cdot X} < 0.1$) and is not dominated by overlap with other gases (Plate 2). Heating by a well-mixed molecule in this nonoverlapped, optically thin limit is constant with air density. In contrast, it is easy to show that in this limit, heating by a well-mixed collision complex (or dimer) increases linearly with air density. The high correlations of the $O_2 \cdot X$ heating in Figure 1 with air density (not shown) confirm that $O_2 \cdot X$ heating obeys the weakly absorbing linear limit in both clear and cloudy skies. The absorbed energy actually increases quadratically with dry air density, i.e., linearly with $O_2 \cdot X$ abundance (1), but one factor of density (the heat capacity of air in J m^{-3} K^{-1}) is removed in converting from a volumetric heating (W m^{-3}) to an absolute heating rate (K d^{-1}). We note that $O_2 \cdot X$ is the only significant solar absorber with this vertical signature. The $O_2 \cdot X$ heating rates in Figure 1 do not appear linear because they are expressed as functions of pressure rather than density.

Figure 1 shows that clouds significantly enhance $O_2 \cdot X$ heating above cloud top and reduce heating beneath cloud top (dotted line). Thus clouds shift the $O_2 \cdot X$ heating profile maximum upward to the level of the cloud top. This feature appears prominently in climatological averages of $O_2 \cdot X$ heating shown in section 4.4.

In summary, $O_2 \cdot X$ bands are present in much of the visible spectrum and in important near-infrared windows. These
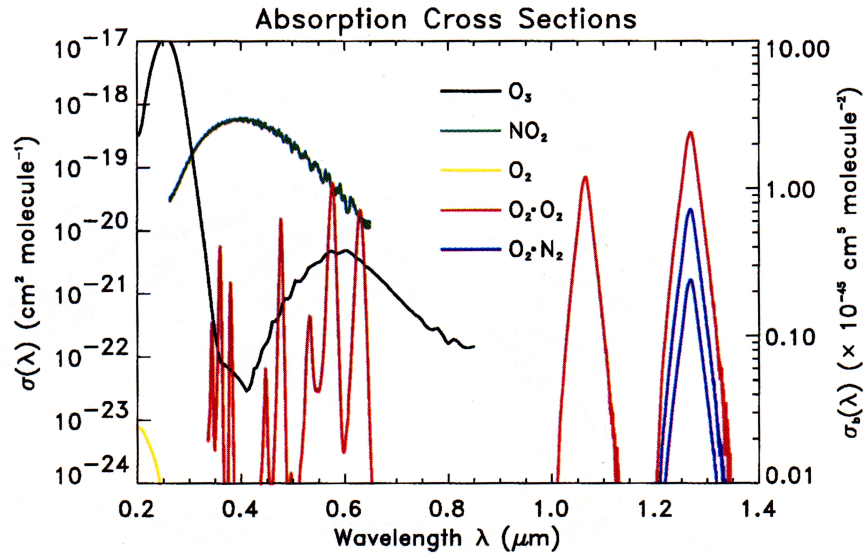
Plate 1. Solar absorption continua of $O_2 \cdot X$, O_3, O_2, and NO_2. Continua of $O_2 \cdot O_2$ (red) and $O_2 \cdot N_2$ (blue) are plotted as binary absorption coefficients $\sigma^b_{O_2 \cdot X}$ (cm^5 molecule^{-2}) on the right-hand axis. Continua of O_3 (black), NO_2 (green), and O_2 (yellow) are plotted as traditional cross sections σ (cm^2 molecule^{-1}) on the left-hand axis.
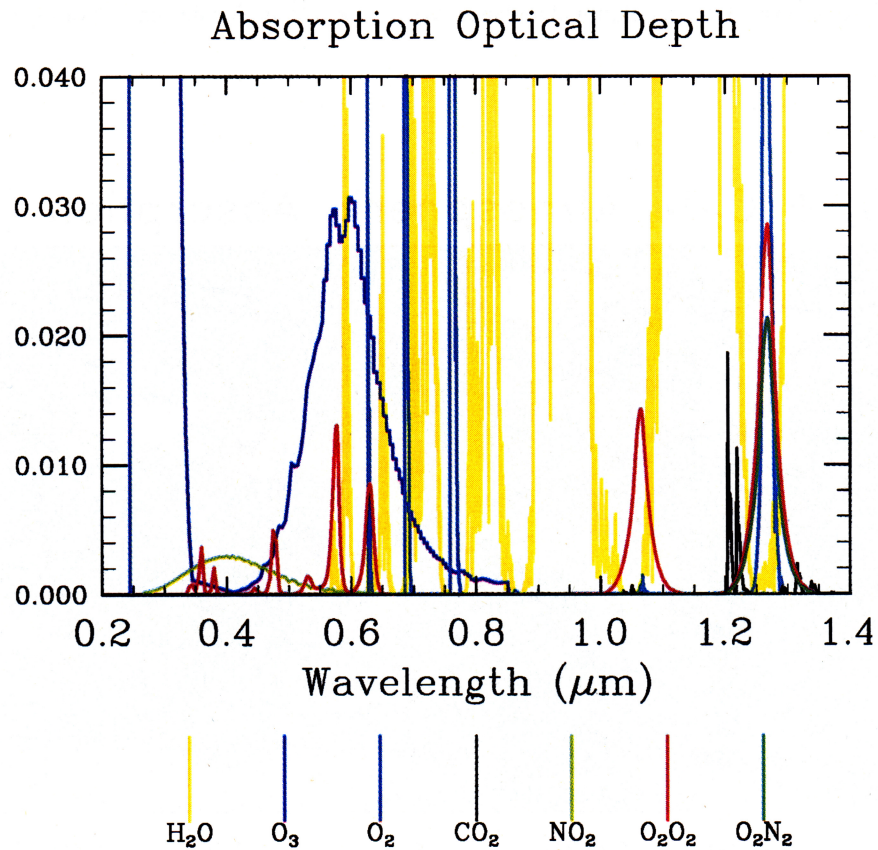

Plate 2. Decomposition of simulated absorption optical depth $\tau_{abs}(\lambda)$ at the CART site at local solar noontime on October 15, 1995. Gaseous absorbers included are $O_2 \cdot O_2$ (red), $O_2 \cdot N_2$ (green), H_2O (yellow), O_3 (blue), O_2 (light blue), NO_2 (light green), and CO_2 (black). The line spectra of H_2O, CO_2, and O_2 are averaged over 10 cm^{-1}.

$O_2 \cdot O_2$ Column ($\times 10^{42}$ molecule^2 cm^{-5})
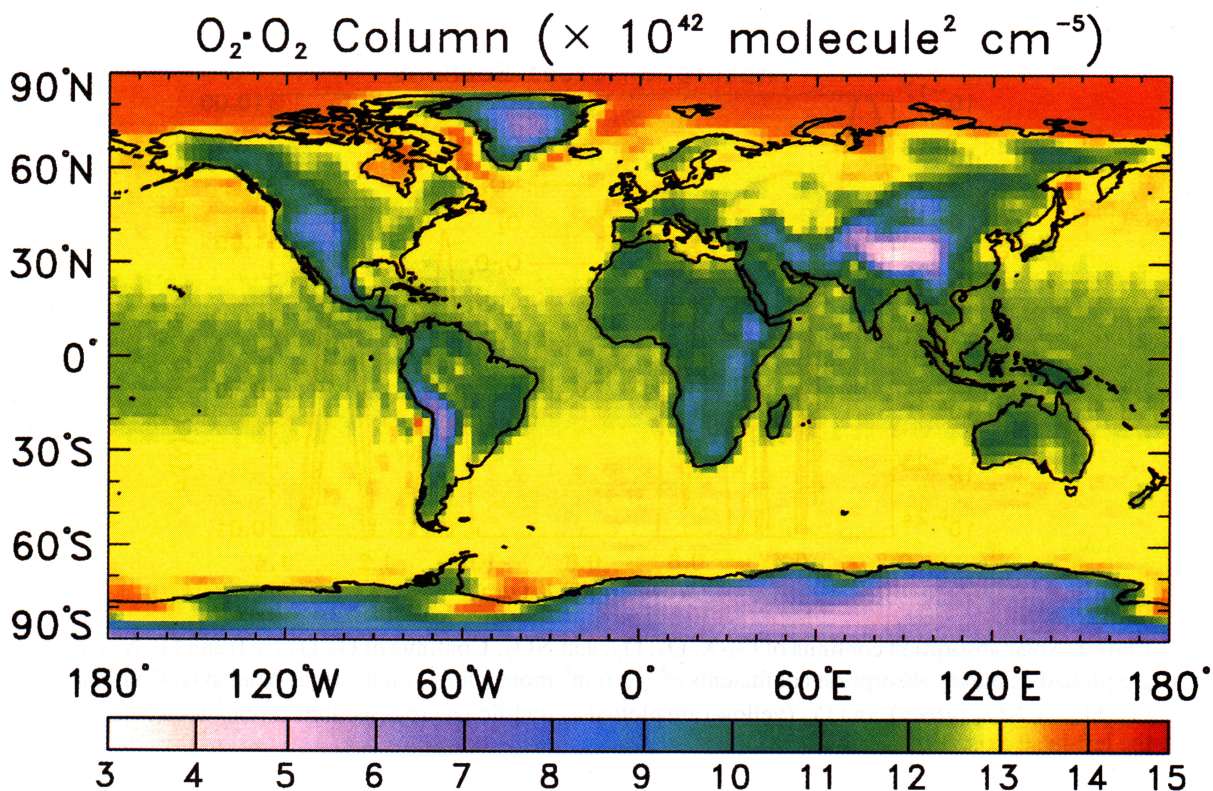
Plate 3. Annual mean column abundance $N_{O_2 \cdot O_2}$ ($\times 10^{42}$ molecule^2 cm^{-5}) of $O_2 \cdot O_2$.

$O_2 \cdot O_2 + O_2 \cdot N_2$ Atmospheric Absorption (W m^{-2})
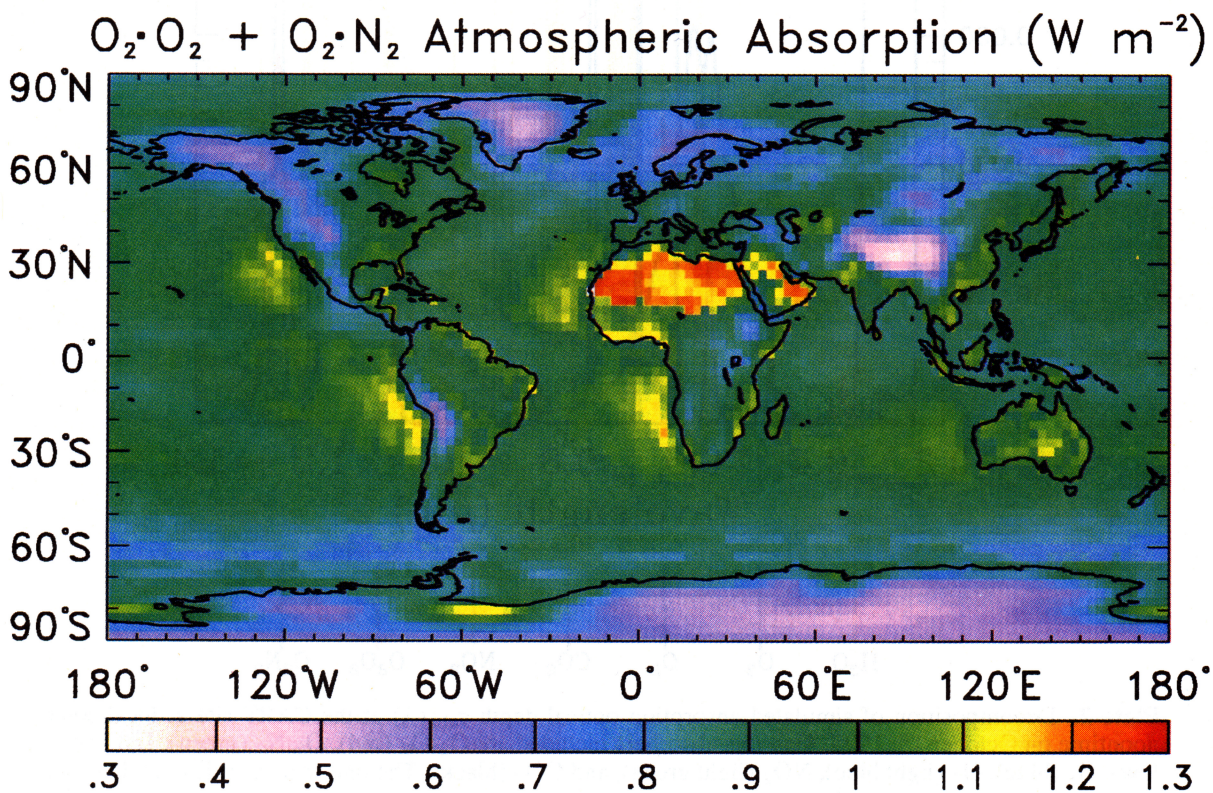
Plate 4. Annual mean increase in column atmospheric absorption (W m^{-2}) due to $O_2 \cdot X$.

a $O_2 \cdot O_2 + O_2 \cdot N_2$ Atmospheric Absorption (W m^{-2}) $O_2 \cdot O_2 + O_2 \cdot N_2$ Atmospheric Absorption (W m^{-2})   **c**

b

d

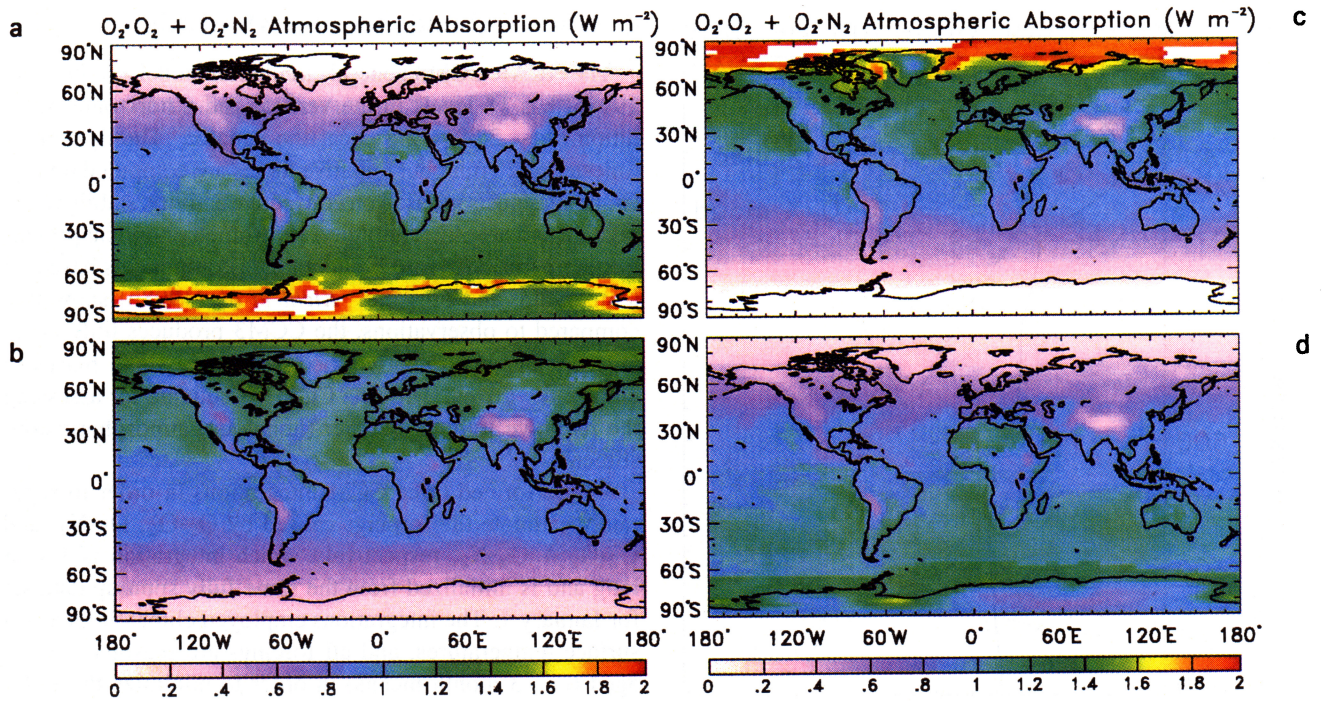**Plate 5.** Seasonal mean increase in atmospheric solar absorption (W m^{-2}) due to O₂·X. (a) December–February (DJF). (b) March–May (MAM). (c) June–August (JJA). (d) September–November (SON). White regions exceed maximum scale value by < 0.7 W m^{-2}.
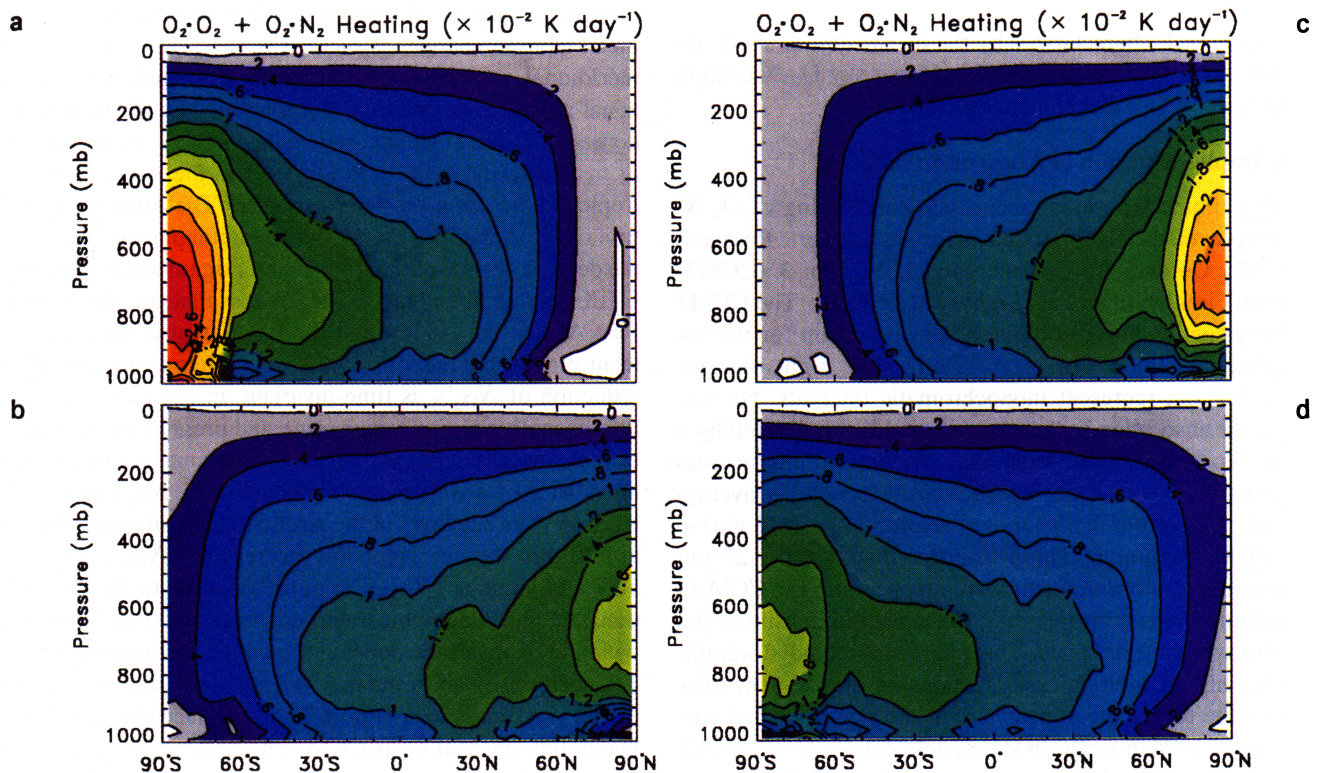
a $O_2 \cdot O_2 + O_2 \cdot N_2$ Heating ($\times 10^{-2}$ K day^{-1}) $O_2 \cdot O_2 + O_2 \cdot N_2$ Heating ($\times 10^{-2}$ K day^{-1})   **c**

b

d

Plate 6. As in Plate 5, but for the vertical profile of the heating ($\times 10^{-2}$ K d^{-1}) due to O₂·X.
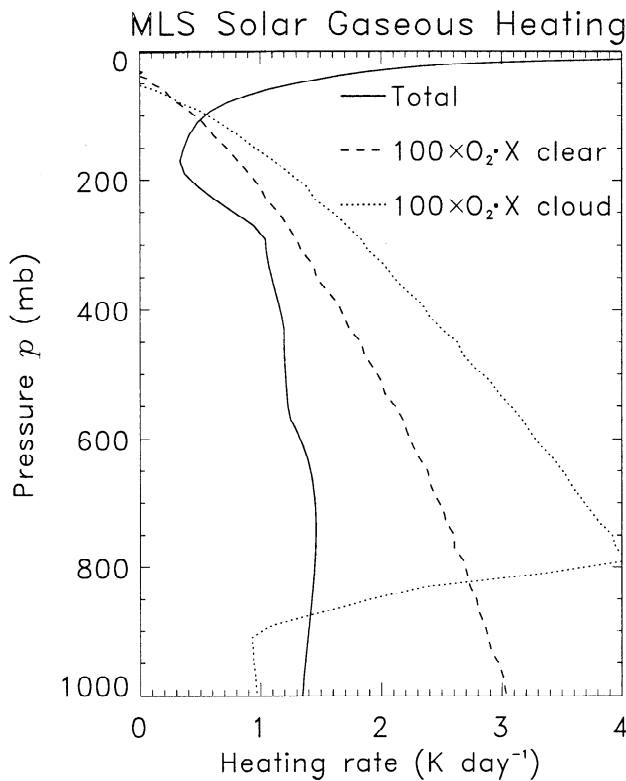
MLS Solar Gaseous Heating

Figure 1. Vertical profile of solar gaseous heating $(K\ d^{-1})$ for a standard, climatological midlatitude summer atmosphere. Shown are the total solar heating rate in clear sky (solid) and, exaggerated by a factor of 100, the O_2-X contributions to the heating in clear sky (dashed) and in the presence of a 100 g m^{-2}, 100 mb thick stratus cloud (dotted).

bands are well characterized by the linear limit of small absorber paths. The vertical profile of clear sky O_2-X heating weakly decreases the atmospheric stability.

3.3. Implementation of Absorption in GCM

To estimate the global abundance and forcing of O_2-X, we employed the National Center for Atmospheric Research (NCAR) Community Climate Model, Version 3 (CCM3) general circulation model [*Kiehl et al.*, 1998a]. The CCM3 employs an 18 bin δ-Eddington approximation for the solar spectral region [*Briegleb*, 1992]. The eight bins for $\lambda < 0.7\ \mu$m represent monochromatic intervals, but water vapor absorption in the near-infrared is represented by a seven bin k-distribution technique. We created binary cross sections $\bar{\sigma}$ for each CCM spectral bin by spectrally averaging $\sigma^b_{O_2\text{-}X}(\lambda)$ from the laboratory resolution (~ 0.15 nm) to the CCM resolution. The near-infrared 1.06 and 1.27 μm continuum absorption bands were mapped into the CCM k-distribution bins corresponding to the mean intensity of the nearest water vapor bands. This procedure included weighting the high-resolution cross sections by the incident solar flux at the top of the atmosphere in the more detailed narrow band multistream (NBM) model [*Zender et al.*, 1997]. In offline single-column comparisons, the CCM3 radiation model and the NBM model O_2-X absorption agreed to within 10% for standard atmospheric conditions ranging from Arctic to Tropical, so no tuning of the $\bar{\sigma}$ was required.

4. Global Abundance and Absorption

The NCAR CCM3 general circulation model [*Kiehl et al.*, 1998a] has 18 levels in the vertical and a horizontal resolution of $\sim 2.8° \times 2.8°$ near the equator. The dynamical timestep is 20 min, but radiative fluxes are computed hourly. Cloud diagnosis is based on convective activity, stability, and relative and absolute humidity. Hydrometeor optical properties are partitioned into liquid and ice components based on temperature and pressure. *Kiehl et al.* [1998b] show that compared to observations, the CCM3 produces little or no bias in clear sky radiative fluxes and only small biases in cloudy sky fluxes. Thus the CCM3 is suitable for assessing the radiative forcing of other (noncloud) atmospheric constituents.

We performed three CCM integrations in order to separately estimate the forcings caused by O_2-O_2, O_2-N_2, and O_2-O_2 + O_2-N_2, respectively. Each integration is 1 year long and is initialized from the same fully spun up data set for January 1. The integrations employed climatological sea surface temperatures, and all forcings are seasonally averaged (i.e., 3 month means) in order to minimize the influence of variability on the results. The solar radiation physics were called twice each solar radiation time step (60 min): once with and once without O_2-X heating. O_2-X forcing is the difference between these values. We archived O_2-X abundance and forcing every times tep (20 min), but these forcings were not allowed to affect the predicted climate.

4.1. Annual Mean Abundance and Absorption

Collision complex abundance is a statistic of the second moment of dry air density (1). Plate 3 shows the annual mean column abundance of O_2-O_2, $N_{O_2 \cdot O_2}$. The major meridional gradient is caused by the poleward decrease in zonal mean temperature. Cold polar air of a given mass is denser than warm tropical air. Since $n_{O_2 \cdot O_2}$ is the square of n_{O_2} (1), $N_{O_2 \cdot X}$ is $\sim 20\%$ greater in the Arctic than the tropics at the same sea level pressure. The same would be true of the Antarctic, except the Antarctic plateau displaces the densest portion of the troposphere, significantly reducing O_2-X column abundance. The Tibetan Plateau, Greenland, East Africa, the Andes, and the Rockies also show significant orographic reduction in $N_{O_2 \cdot X}$. Note that orographic reduction of $N_{O_2 \cdot X}$ is time-invariant, in contrast to effects of seasonally varying temperature and pressure in the extratropics, discussed below. Whereas the zonal mean column abundance of a well-mixed molecule (e.g., N_{O_2}) decreases by 30% from sea level in the Arctic to the Antarctic plateau at 700 mb, the corresponding decrease in $N_{O_2 \cdot X}$ exceeds 50%. In summary, O_2-X is more sensitive to the thermodynamic and orographic environment than O_2 or N_2 alone, owing to its quadratic dependence on these constituents.

Uncertainties in simulated $N_{O_2 \cdot X}$ stem from biases in model pressure p, temperature T, and surface elevation. The maximum seasonal mean CCM temperature bias in the lower troposphere is < 6 K [*Hack et al.*, 1998]. The maximum seasonal mean CCM grid point surface pressure bias is $< 1\%$ [*Hurrell et al.*, 1998]. Biases in column O_2 arising from the discretization of surface elevation do not ex-

ceed 1%. Assuming the worst case scenario (errors are additive) yields a conservative uncertainty in seasonal grid point mean N_{O_2} and N_{N_2} of $\pm 4\%$, implying uncertainty bounds for $N_{O_2 \cdot O_2}$ and $N_{O_2 \cdot N_2}$ of $\pm 8\%$. The maximum uncertainty is over the Antarctic shelf and the Tibetan Plateau, regions where variability and differences with climatological analyses are relatively large [*Hurrell et al.*, 1998]. The simulated annual mean surface pressure is 984.5 mb, in excellent agreement with 984.9 mb from National Centers for Environmental Prediction (NCEP) reanalyses. This confirms that grid point biases in $N_{O_2 \cdot X}$ are generally random, not systematic, and we place the global mean bias conservatively at $\pm 2\%$. As will be described below, grid point biases in simulated $O_2 \cdot X$ forcing are generally dominated by uncertainties in absorber cross section and cloud vertical distribution, not $O_2 \cdot X$ abundance.

The regional abundance of any well-mixed collision complex $X \cdot Y$ is determined by scaling Plate 3 by the product of the ratios n_X / n_{O_2} and n_Y / n_{O_2}. Table 1 summarizes the scale factors (relative to $O_2 \cdot O_2$) and global annual mean abundances of many well-mixed collision complexes. The scale factors were computed using atmospheric abundances of *Goody and Yung* [1989, p. 9], corrected to present-day values in the case of CO_2 (355 ppm) and CH_4 (1.7 ppm).

The final column of Table 1 lists the approximate centers of the collision induced absorption bands due to each complex, apart from the $O_2 \cdot X$ bands shown in Plate 1. Taken together, such bands appear in the spectrum from the Herzberg continuum to the far infrared. In addition to the bands shown in Plate 1, collisions involving $O_2 \cdot O_2$ and $O_2 \cdot N_2$ induce oxygen absorption in the Herzberg continuum from 195 to 250 nm and in the oxygen (forbidden) fundamental vibration band at 6.42 μm [*Shardanand and Rao*, 1977; *Orlando et al.*, 1991]. Both $O_2 \cdot N_2$ and $N_2 \cdot N_2$ induce absorption in the nitrogen (forbidden) fundamental band at 4.29 μm. Insolation in these spectral regions is too weak to allow significant solar absorption in absolute terms. However, it may be important to account for this absorption when retrieving atmospheric parameters such as temperature from remotely sensed spectra, for example, in the CO_2 4.3 μm band [*Goody and Yung*, 1989, p. 192].

Plate 4 shows the annual mean increase in atmospheric absorption due to $O_2 \cdot X$. The annual mean forcing approximately resembles the abundance (Plate 3), though some new features are evident. First note the enhanced atmospheric absorption above bright, low surfaces (desert, stratus clouds, ice). Since the spectral optical depth of most $O_2 \cdot X$ bands is < 0.05 (Plate 2), absorption in these bands is in the linear limit where a change in absorber path causes a proportionate change in atmospheric absorption. Reflection from low, bright surfaces increases photon path lengths in the $O_2 \cdot X$-rich lower atmosphere. This increases the mean $O_2 \cdot X$ path and thus the $O_2 \cdot X$ absorption. However, reflection from high clouds (e.g., tropical cirrus) prevents photons from reaching the lower atmosphere and reduces the mean $O_2 \cdot X$ path traversed by these photons. This reduces $O_2 \cdot X$ absorption and causes the local minima in $O_2 \cdot X$ forcing in the Intertropical Convergence Zone (ITCZ) region. The zonal annual mean atmospheric absorption due to $O_2 \cdot X$ is ~ 0.9 W m^{-2} and does not vary strongly with latitude (not shown).

It is interesting to note that geographic structure of $O_2 \cdot N_2$ absorption closely resembles that of $O_2 \cdot O_2$ absorption, so that their sum, Plate 4, adequately represents the structure of each. Since $O_2 \cdot N_2$ absorption occurs entirely in the 1.27 μm band, it is enhanced relative to $O_2 \cdot O_2$ over vegetated surfaces but diminished over sea-ice and ocean due differences between the near-infrared and visible albedos of these surfaces. The magnitude of global mean $O_2 \cdot N_2$ absorption is proportional to the assumed N_2 efficiency. This study assumes $\epsilon_{N_2} = 0.2$, which leads to $O_2 \cdot N_2$ forcing being 20% of $O_2 \cdot O_2$ absorption. As discussed in section 2.2, ϵ_{N_2} may be 0.3, in which case $O_2 \cdot N_2$ forcing would be 30% of $O_2 \cdot O_2$ forcing.

It is useful to distinguish atmospheric absorption from other common metrics of radiative forcing. Table 2 summarizes the global mean statistics of $O_2 \cdot X$ atmospheric forcing, surface forcing, column radiative forcing, and net radiative forcing at the tropopause. The first row, atmospheric forcing, is the mean increase in atmospheric absorption due to $O_2 \cdot X$ (Plate 4), 0.93 W m^{-2}. For comparison, the all sky solar absorption due to H_2O, O_3, O_2, and CO_2 is ~ 43, 14,

Table 1. Global Annual Mean Abundances of Well-Mixed Collision Complexes

Complex $X \cdot Y$	Scale $N_{X \cdot Y} / N_{O_2 \cdot O_2}$	Abundance, molecule^2 cm^{-5}	Collision Induced Absorption Bands
$O_2 \cdot O_2$	1	1.24×10^{43}	HC, 1.58 μm 6.42 μm
$O_2 \cdot N_2$	3.728	4.62×10^{43}	HC, 4.29 μm, 6.42 μm, 100 cm^{-1}
$N_2 \cdot N_2$	13.90	1.72×10^{44}	4.29 μm, 90 cm^{-1}
$O_2 \cdot Ar$	0.0446	5.52×10^{41}	HC, 1.27 μm, 6.42 μm
$O_2 \cdot CO_2$	1.69×10^{-3}	2.09×10^{40}	1.27 μm
$O_2 \cdot CH_4$	8.1×10^{-6}	1.00×10^{38}	HC
$CO_2 \cdot CO_2$	2.87×10^{-6}	3.55×10^{37}	60 cm^{-1}

Scale factors relate $N_{X \cdot Y}$ to $N_{O_2 \cdot O_2}$ (1). Band locations are approximate centers of absorption bands. HC denotes Herzberg Continuum (~ 200–250 nm). $O_2 \cdot O_2$ and $O_2 \cdot N_2$ bands considered in this study (Plate 1) are omitted for brevity. Spectral data compiled from *Shardanand* [1977], *Shardanand and Rao* [1977], *Goody and Yung* [1989], *Orlando et al.* [1991], *Oshima et al.* [1995], *Solomon et al.* [1998], and *Mlawer et al.* [1998].

Table 2. Global Annual Mean Forcings of O_2-X

Forcing, W m^{-2}	$O_2 \cdot O_2$	$O_2 \cdot N_2$	Total
Atmospheric Absorption	0.78	0.15	0.93
(same, but for clear sky)	(0.78)	(0.17)	(0.94)
Surface Insolation	−0.50	−0.10	−0.60
Surface Absorption	−0.42	−0.08	−0.51
Sfc. + Atm. Absorption	0.36	0.07	0.42
Net Flux at Tropopause	0.34	0.06	0.40

Total forcings may be up to 20% lower or 30% higher than indicated. See text for uncertainty analysis. Sfc, surface; Atm, atmosphere.

2, and 0.5 W m^{-2}, respectively [*Kiehl and Trenberth*, 1997] (NO_2 abundance is highly heterogeneous and a reliable estimate of its mean absorption has yet to be made). The second row shows that on average, the clear sky atmospheric absorption by O_2-X slightly exceeds the all sky absorption.

Atmospheric absorption at solar wavelengths reduces surface insolation (third row of Table 2) and thus surface absorption (fourth row). The fifth row shows the column radiative forcing, the sum of atmospheric forcing and surface forcing. This quantity (column radiative forcing) equals the change in net radiative flux at the top of the atmosphere. The impact of atmospheric constituents on tropospheric climate is, by convention, quantified by the change in net radiative flux at the tropopause, shown in row six. More than 97% of O_2-X, and thus 97% of O_2-X absorption, is in the troposphere (see Plate 6). Therefore the column radiative forcing of O_2-X nearly equals the net radiative forcing at the tropopause.

4.2. Uncertainty in Mean O_2-X Forcing

The largest uncertainties in the estimates in Table 2 stem from uncertainties in cross section $\sigma^b_{O_2 \cdot O_2}$, N_2 efficiency ϵ_{N_2}, O_2-X abundance $N_{O_2 \cdot X}$, and cloud vertical distribution. The uncertainty ranges for these quantities are $\sigma^b_{O_2 \cdot O_2}(\lambda)$, −30 to +10%, depending on λ (see section 2.2); ϵ_{N_2}, ±50%; and $N_{O_2 \cdot X}$, ±2%. Also, appending the $O_2 \cdot O_2$ 1.58 μm continuum of *Mlawer et al.* [1998] to the *Solomon et al.* [1998] cross sections would increase our computed total O_2-X solar forcing by ∼ 4%. As discussed in section 2.1, the possible temperature dependence of $\sigma^b_{O_2 \cdot X}(\lambda)$ is not yet fully understood [*Greenblatt et al.*, 1990; *Newnham and Ballard*, 1998; *Osterkamp et al.*, 1998]. Therefore we have not included uncertainty due to possible temperature dependence of $\sigma^b_{O_2 \cdot X}$ in our error analysis.

The simulated mean clear sky and all sky planetary albedos agree with satellite observations to within 0.005 [*Hack et al.*, 1998], eliminating the possibility of gross surface or cloud reflectance biases in estimated O_2-X forcing. Modeled total cloud fraction, 0.588, is bracketed by the Nimbus 7 and International Satellite Cloud Climatology Project (ISCCP) estimates of 0.522 and 0.625, respectively [*Hack et al.*, 1998]. The vertical distribution of cloudiness generally agrees with observations for clouds below 400 mb but disagrees for cloud top heights above 400 mb, a region where clouds efficiently reduce O_2-X forcing. The CCM

high cloud fraction, 0.34, exceeds ISCCP analyses by 0.20 [*Hack et al.*, 1998]. There is considerable uncertainty in the observations, but if the ISCCP total and high cloud estimates are correct, then we estimate the modeled all sky O_2-X forcing is up to 10% too low because of exaggerated amounts of high-level cloud relative to low-level cloud.

Except for O_2-X abundance, the aforementioned uncertainties are systematic, not random. Summing the uncertainties for a conservative error estimate yields a total uncertainty range for the all sky forcings in Table 2 of −20 to +30%. Thus the uncertainty range for O_2-X all sky absorption is 0.75–1.21 W m^{-2}. The lower bound forcing corresponds to the 1.06 and 1.27 μm $\sigma^b_{O_2 \cdot X}$ of *Mlawer et al.* [1998] and N_2 efficiency $\epsilon_{N_2} = 20\%$ (3). The upper bound forcing uses $\sigma^b_{O_2 \cdot X}$ from *Greenblatt et al.* [1990] and *Solomon et al.* [1998], $\epsilon_{N_2} = 30\%$, and assumes that 4% of O_2-X absorption occurs at 1.58 μm and that the CCM3 overpredicts high level clouds relative to low-level clouds.

The results in Table 2 appear to contrast with two prior studies. *Pfeilsticker et al.* [1997] estimate $O_2 \cdot O_2$ enhances all sky heating relative to clear sky heating by ∼ 7% (neglecting the 1.27 μm band). Using identical O_2-X cross sections to our study, *Solomon et al.* [1998] estimated the mean atmospheric absorption due to O_2-X is 0.9–1.3 W m^{-2}. Both these prior studies used the same method to convert single-column results to global mean results. The method assumes 50% of the globe is covered with cloud top heights at 700 mb and that these clouds increase the photon path by 30 km [*Pfeilsticker et al.*, 1997]. Thus their conversion method assumes fewer and lower clouds than predicted by the CCM3. These assumptions both lead to larger forcings than shown in Table 2 and, taken together, suffice to explain the differences between the studies. It is unclear whether assumptions regarding surface albedo and elevation also contribute to these model differences.

4.3. Seasonal Structure of Abundance and Absorption

Owing to the seasonal cycles of insolation and temperature, annual mean forcings do not suffice to characterize the geographic and vertical distribution of O_2-X forcing as it impacts the climate system. To illustrate this point, Figure 2 shows the zonal mean of the column abundance of $O_2 \cdot O_2$ for December–February (DJF) and June–August (JJA). The increases in $N_{O_2 \cdot X}$ from summer to winter in the North and South polar regions are 8–10% and 1–3%, respectively. These increases are entirely due to seasonal changes of pressure and temperature. Although the solar radiative forcing of O_2-X during polar winter is zero, this seasonal cycle in $N_{O_2 \cdot X}$ does affect O_2-X absorption bands in the far infrared (see Table 1) throughout the year. The meridional gradient and seasonal changes in $N_{O_2 \cdot X}$ depicted in Figure 2 apply to all other collision complexes in Table 1 as well.

The strongest modulator of solar radiative forcing is, of course, the seasonal change of insolation. Plate 5 shows the geographic distribution of the seasonal mean atmospheric absorption by O_2-X. O_2-X absorption is greatest in polar regions in summer, where peak insolation coincides with the greatest O_2-X abundances (Figure 2). Plates 5a
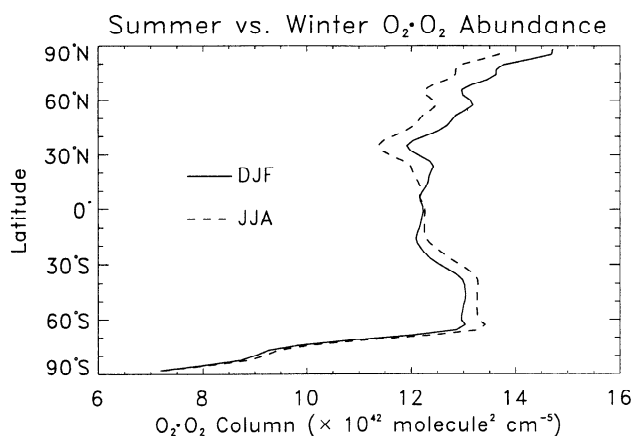
Figure 2. Zonal mean column abundance of O_2·O_2, $N_{O_2·O_2}$ ($\times 10^{42}$ molecule^2 cm^{-5}), for DJF (solid line) and JJA (dashed line).

and 5c show southern and northern summer forcings are nearly symmetric about the equator. Arctic forcing is 10–30% stronger than Antarctic forcing, mainly the Antarctic plateau reduces $N_{O_2·X}$. Most remarkable are the large polar regions where atmospheric O_2·X absorption approaches or exceeds 2.0 W m^{-2} on seasonal timescales. Seasonal sea ice boundaries appear in Plates 5a–5d where they demarcate the open ocean from regions of higher absorption. Equinoctial forcings (Plates 5b and 5d) extend farther into the winter hemisphere than solstitial forcings, and are weaker.

Surface albedo, elevation, and clouds all play roles in determining the seasonal forcing maxima near the poles. To help disentangle these roles, we show in Figure 3 the zonal mean of the winter and summer seasonal forcings (Plates 5a and 5c) due to O_2·X. The influence of clouds and surface albedo on O_2·X forcing is clarified by comparing the seasonal forcings in Figure 3 to the seasonal abundances in Figure 2. The zonal mean summertime O_2·X forcing in the Antarctic (70–90°S), 1.69 W m^{-2}, is 96% of the forcing in the Arctic (70–90°N), 1.76 W m^{-2}, although the Antarctic has only 74% of the O_2·X. Thus surface and low-level cloud reflectance makes O_2·X forcing 30% more efficient (per unit abundance) in the Antarctic than in the Arctic. Within 5° of the poles, the forcing efficiency of O_2·X is 75% greater in the Antarctic than in the Arctic. The change in forcing efficiency reduces, and nearly eliminates, the surface elevation-induced disparity in forcing between the poles.

The large difference between the forcing efficiencies of O_2·X in the Arctic and the Antarctic is caused by differences in the surface albedo, cloud distribution, and water vapor column between the two polar climate systems. First, the simulated visible surface albedo of Arctic sea ice is $\sim$ 0.6, much lower than the simulated visible surface albedo of the Antarctic continent, $\sim$ 0.95 [Briegleb and Bromwich, 1998a]. Offline sensitivity studies show that in the absence of clouds, the higher surface reflectance underlying Antarctic O_2·X increases forcing (per unit abundance) by $\sim$ 25% relative to the Arctic. Observations suggest the modeled surface albedo and low-level cloud fraction in the summertime

Arctic are $\sim$ 0.15 and 0.10 too high, respectively [Briegleb and Bromwich, 1998a]. This suggests the simulated summertime Arctic forcing is too high, which would amplify the disparity between Arctic and Antarctic forcing efficiencies.

A second, but much weaker, effect is due to the change in simulated precipitable water content from the summertime Arctic (11.5 kg m^{-2}) to the Antarctic (2.7 kg m^{-2}). Both are in fair agreement with European Centre for Medium-Range Weather Forecasts (ECMWF) analyses [Briegleb and Bromwich, 1998a]. The drier Antarctic column makes the wings of the near-infrared water vapor bands (compare Plate 2) more transmissive (less saturated). This increases absorption per unit O_2·X by $\sim$ 2%.

4.4. Vertical Structure

The vertical profile of O_2·X heating is important in determining possible dynamical feedbacks as well as the change in net flux at the tropopause. Plate 6 shows the vertical profile of the seasonally and zonally averaged solar heating due to O_2·X. The vertical axis is the CCM hybrid vertical coordinate times 1000 [Kiehl et al., 1998a]. Thus the panels transition from a pure sigma coordinate representation at the surface to a pure pressure representation near 200 mb. As mentioned previously, virtually all of the heating is confined to the troposphere. O_2·X heating decreases toward the winter hemisphere due to decreasing daylight hours. Above 700 mb (300 mb above the surface) the heating decreases with pressure due to decreasing O_2·X abundance (compare Figure 1). Seasonal O_2·X heating in excess of 0.02 K d^{-1} extends throughout the polar summer troposphere. This is 2–4% of local solar heating owing to all other solar absorbers (compare Figure 1). The heating rate in the Antarctic summer troposphere (Plate 6a) is nearly 20% stronger than the Arctic summer troposphere (Plate 6c) due to its thinner at-

The heating peaks between 200–300 mb above the surface in all regions every season. This peak does not coincide with the maximum O_2·X abundance (which is always at the surface) even though O_2·X absorption is in the opti-
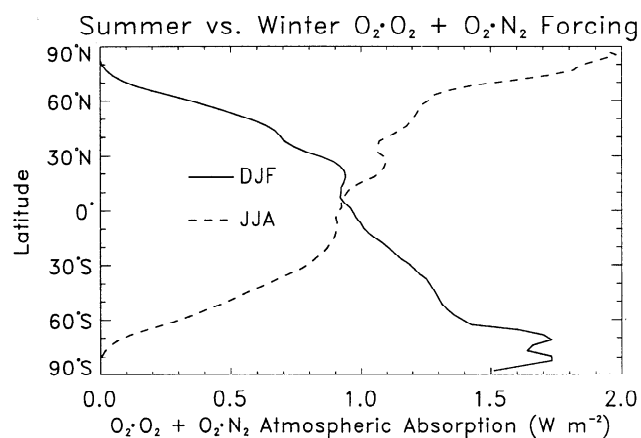

Figure 3. Zonal seasonal mean increase in atmospheric solar absorption (W m^{-2}) due to O_2·X: DJF (solid line) and JJA (dashed line).

cally thin limit (Plate 2). As shown in Figure 1, the location of maximum $O_2 \cdot X$ heating does coincide with maximum $O_2 \cdot X$ abundance except when efficient scatterers such as clouds screen the $O_2 \cdot X$ in the lower atmosphere from incoming solar radiation. Thus cloud reflection is responsible for shifting the mean vertical location of maximum $O_2 \cdot X$ absorption, and thus heating, upward from the surface by 200–300 mb. Plate 6 supports this by showing that the heating maxima as a function of latitude dips somewhat closer to the surface in the subtropical regions characterized by large-scale subsidence and relatively clear skies.

Radiative forcing in other nonoverlapped, optically thin bands of well-mixed collision complexes (e.g., the $N_2 \cdot N_2$ fundamental band at 4.29 μm, see Table 1), will show qualitatively similar patterns to Plates 4–6. The magnitude of forcing by other bands is, of course, highly sensitive to the spectral location of the particular band.

5. Discussion and Summary

We have characterized the spectral, vertical, regional, and seasonal atmospheric heating by $O_2 \cdot X$. The motivations for modeling the global distribution and forcing of $O_2 \cdot X$ were to refine and extend estimates of $O_2 \cdot X$ forcing inferred from one-dimensional studies to the global climate scale. Our global simulations indicate that global annual mean atmospheric absorption by $O_2 \cdot X$ is 0.75–1.2 W m^{-2} (Table 2). This falls between the recent estimates of 0.9–1.3 W m^{-2} [*Solomon et al.*, 1998] and 0.84 W m^{-2} [*Mlawer et al.*, 1998]. This absorption reduces surface insolation by 0.48–0.78 W m^{-2}.

$O_2 \cdot X$ absorption is highly localized in the troposphere and it increases the net radiative flux at the tropopause by 0.32–0.52 W m^{-2}. It is useful to compare this absolute radiative forcing by $O_2 \cdot X$ (whose abundance is not changing) to greenhouse gas forcing (due to changes in the gases' abundance from preindustrial to present-day levels). This comparison enables us to assess the magnitude of the perturbation to the mean state climate caused by $O_2 \cdot X$. The 0.32–0.52 W m^{-2} forcing by $O_2 \cdot X$ is less than the anthropogenic forcing of CO_2 (1.75 W m^{-2}) but comparable to forcing by CH_4 (0.44 W m^{-2}), stratospheric H_2O (0.15 W m^{-2}), and N_2O (0.11 W m^{-2}) [*Shine et al.*, 1990, p. 57].

By extending the simulations to the global scale, we were able to characterize the spatial and temporal distributions of $O_2 \cdot X$ abundance and forcing. $O_2 \cdot X$ abundance mimics the concentration of O_2 and N_2, except its quadratic dependence on these constituents accentuates both its spatial and temporal gradients. This dependence causes a 20% increase in $O_2 \cdot X$ abundance in the Arctic relative to the Tropics for the same sea level pressure. $O_2 \cdot X$ abundance depends most on zonal mean temperature, pressure, and surface elevation. The variations in zonal mean $O_2 \cdot X$ abundance due to surface elevation, the annual mean meridional temperature gradient, and to seasonal temperature variations are 40, 15, and 10%, respectively. These results scale to all collision complexes of well-mixed gases, for example, $N_2 \cdot N_2$ and $O_2 \cdot Ar$.

Many features of $O_2 \cdot X$ radiative forcing are common to all solar absorbers, but the relatively sharp gradients in

$O_2 \cdot X$ abundance enhance these features. Surface and cloud reflectance modulate the solar forcing efficiency of $O_2 \cdot X$ (forcing per unit abundance) by altering the mean $O_2 \cdot X$ path traversed by the average photon. These factors explain why annual mean collision complex forcing peaks in the subtropics over bright deserts and regions of marine stratus. The seasonal cycle of insolation causes the seasonal mean solar forcing to peak in summertime polar regions. However, these summertime polar peaks are enhanced by bright surfaces and extensive low-level clouds, especially in the Arctic. The forcing efficiency of complexes in the Antarctic is 30–75% greater than in the Arctic.

In clear skies the magnitude of $O_2 \cdot X$ heating grows linearly with air density, peaking at the surface. This heating profile tends to weakly destabilize the atmospheric column. On seasonal timescales, clouds shift the height of peak $O_2 \cdot X$ heating upward by 200–300 mb and smooth out the vertical decrease of heating that would otherwise follow the rapid decrease of $O_2 \cdot X$ abundance with height. $O_2 \cdot X$ heating peaks at 0.02–0.03 K d^{-1} in the polar troposphere in summer. This is 2–4% of local heating due to all other solar absorbers.

Many GCMs have strong cold biases at the summertime polar tropopause, where the CCM3 (not shown) is up to 10–14 K too cold [*Hack et al.*, 1998]. The CCM3 also suffers from a cold bias in the summertime polar troposphere of 2–6 K [*Briegleb and Bromwich*, 1998b]. Some, but probably not all, of these biases are due to the numerical treatment of dynamics [*Williamson and Olson*, 1998]. It is likely that allowing $O_2 \cdot X$ heating to affect the thermal structure of the atmosphere will ameliorate, though not eliminate, the remainder of these biases. For example, single-column simulations show the radiative relaxation timescale at the polar tropopause is $\sim$ 50 days. Thus the $O_2 \cdot X$ heating of $\sim$ 0.01 K d^{-1} (Plate 6) increases the radiative equilibrium temperature by $\sim$ 1 K in this region.

We quantified some fingerprints that distinguish absorption due to well-mixed collision complexes (and well-mixed dimers) from absorption due to well-mixed monomers. The most significant distinguishing feature is the stronger spatial and temporal gradients of collision complex abundance relative to monomer abundance. Whereas the zonal mean column abundance of a well-mixed molecule such as O_2 decreases by 30% from sea level in the Arctic to the Antarctic plateau at 700 mb, the corresponding decrease in $N_{O_2 \cdot X}$ exceeds 50%. In the weakly absorbing, nonoverlapped limit, well-mixed molecules cause an increase in the solar heating rate that is constant with air density, whereas well-mixed collision complexes such as $O_2 \cdot X$ cause the solar heating rate to increase linearly with air density.

Zender et al. [1997] demonstrated that $O_2 \cdot O_2$ absorption improved agreement between modeled and observed solar absorption in both clear and cloudy skies during the Atmospheric Radiation Measurement (ARM) Enhanced Shortwave Experiment (ARESE). Their total (direct + diffuse) clear sky surface insolation discrepancies ($\sim$ 15 W m^{-2}) were no larger than instrumental and model uncertainties (e.g., aerosol properties). Working with an independent set of radiometric observations from ARESE, *Kato et al.* [1997] found excellent model agreement with direct beam observa-

tions but reported a 30 W m^{-2} model overestimate of the instantaneous diffuse surface insolation during clear sky conditions over multiple days during ARESE. They did not account for $O_2 \cdot X$ absorption. As shown in section 3.1, $O_2 \cdot X$ absorption reduced clear sky noontime surface insolation by $\sim$ 2 W m^{-2} during ARESE. However, nearly 90% of this $O_2 \cdot X$ absorption came from the direct solar beam, and only 10% occurred in the diffuse field. This illustrates the point that unknown or neglected gaseous absorption processes cannot, by themselves (i.e., without invoking aerosol processes), remedy a clear sky diffuse radiation bias because gaseous absorption of the direct beam far exceeds gaseous absorption of the diffuse field.

Our global simulations show that in the annual mean, $O_2 \cdot X$ enhances absorption equally in clear and cloudy skies. Thus $O_2 \cdot X$ neither exacerbates nor remediates solar absorption discrepancies that are associated with clouds [*Stephens and Tsay*, 1990; *Cess et al.*, 1995; *Ramanathan and Vogelmann*, 1997]. The agreement between clear and cloudy sky $O_2 \cdot X$ absorption is due to the global mean cancellation of photon and absorber path length changes due to clouds: Low-level clouds increase $O_2 \cdot X$ absorption relative to clear skies by increasing path lengths, while middle- and high-level clouds decrease $O_2 \cdot X$ absorption by screening photons from the lower atmosphere. We hypothesize that this agreement is predominantly due to the global vertical distributions of cloud reflectivity and well-mixed molecules and has little to due with spectral features particular to $O_2 \cdot X$. There are two reasons to expect that this hypothesis is true. First, $O_2 \cdot X$ absorption occurs at many locations in the visible and near-infrared and is not correlated with water vapor or condensate absorption bands. Second, cloud transmission is nearly spectrally uniform for $0.3 < \lambda < 1.5$ μm, so clouds do not preferentially transmit any energetically significant solar wavelength bands to the lower atmosphere. This hypothesis should be tested because, if it is true, it implies that globally averaged, well-mixed collision complexes or dimers do not enhance absorption more in cloudy sky than in clear sky. A similar hypothesis may hold for well-mixed molecules in general.

The radiative importance of other abundant, but not necessarily well-mixed, collision complexes and dimers in the atmosphere should be explored. *Solomon et al.* [1998] point out that Ar and CO_2 are also relatively efficient partners for inducing O_2 absorption at 1.27 μm but note that $O_2 \cdot$Ar and $O_2 \cdot CO_2$ are too scarce (Table 1) to cause significant absorption. *Chýlek and Geldart* [1997] and *Solomon et al.* [1998] suggest $O_2 \cdot H_2O$ and $(H_2O)_2$ as promising candidates to examine in the search for neglected solar absorbers.

In summary, the recent discovery that the oxygen collision pairs $O_2 \cdot O_2$ and $O_2 \cdot N_2$ absorb a small but significant fraction of the globally incident solar radiation alters the long-standing view that H_2O, O_3, O_2, CO_2, and NO_2 are the only significant gaseous solar absorbers in Earth's atmosphere. This study quantified the spectral, regional, vertical, and seasonal patterns of $O_2 \cdot X$ abundance and radiative forcing. We now know that globally and annually averaged, $O_2 \cdot X$ absorbs about 1 W m^{-2} of solar radiation, more than CO_2, and that $O_2 \cdot X$ does not increase cloudy

sky solar absorption relative to clear sky absorption. Improved measurements of $O_2 \cdot X$ absorption cross sections in the near infrared will remove about half of the 25% uncertainty in total $O_2 \cdot X$ absorption. Accounting for $O_2 \cdot X$ reduces discrepancies between models and measurements of solar absorption. $O_2 \cdot X$ absorption should therefore be included in high-resolution radiative transfer models, remote-sensing retrieval algorithms, and in large-scale atmospheric models used to simulate climate and climate change. $O_2 \cdot X$ has the most potential to improve the simulated climate in summertime polar regions. Future versions of the CCM will include this absorption.

References

Briegleb, B. P., Delta-Eddington approximation for solar radiation in the NCAR community climate model, *J. Geophys. Res.*, *97*, 7603–7612, 1992.

Briegleb, B. P., and D. H. Bromwich, Polar radiation budgets of the NCAR CCM3, *J. Clim.*, *11*, 1246–1269, 1998a.

Briegleb, B. P., and D. H. Bromwich, Polar climate simulation of the NCAR CCM3, *J. Clim.*, *11*, 1270–1286, 1998b.

Cess, R. D., et al., Interpretation of cloud-climate feedback as produced by 14 atmospheric general circulation models, *Science*, *245*, 513–516, 1989.

Cess, R. D., et al., Absorption of solar radiation by clouds: Observations versus models, *Science*, *267*, 496–499, 1995.

Chýlek, P., and D. J. W. Geldart, Water vapor dimers and atmospheric absorption of electromagnetic radiation, *Geophys. Res. Lett.*, *24*, 2015–2018, 1997.

Collins, W. D., A global signature of enhanced shortwave absorption by clouds, *J. Geophys. Res.*, *103*, 31669–31679, 1998.

Conant, W. C., V. Ramanathan, F. P. J. Valero, and J. Meywerk, An examination of the clear-sky solar absorption over the Central Equatorial Pacific: Observations versus models, *J. Clim.*, *10*, 1874–1884, 1997.

Davidson, J. A., C. A. Cantrell, A. H. McDaniel, R. E. Shetter, S. Madronich, and J. G. Calvert, Visible-ultraviolet absorption cross sections for NO_2 as a function of temperature, *J. Geophys. Res.*, *93*, 7105–7112, 1988.

Erle, F., K. Pfeilsticker, and U. Platt, On the influence of tropospheric clouds on zenith-scattered-light measurements of stratospheric species, *Geophys. Res. Lett.*, *22*, 2725–2728, 1995.

Goody, R. M., and Y. L. Yung, *Atmospheric Radiation Theoretical Basis*, 2nd ed., Oxford Univ. Press, New York, 1989.

Greenblatt, G. D., J. J. Orlando, J. B. Burkholder, and A. R. Ravishankara, Absorption measurements of Oxygen between 330 and 1140 nm, *J. Geophys. Res.*, *95*, 18577–18582, 1990.

Hack, J. J., J. T. Kiehl, and H. W. Hurrell, The hydrologic and thermodynamic characteristics of the NCAR CCM3, *J. Clim.*, *11*, 1151–1178, 1998.

Halthore, R. N., S. Nemesure, S. E. Schwartz, D. G. Imre, A. Berk, E. G. Dutton, and M. H. Bergin, Models overestimate diffuse clear-sky surface irradiance: A case for excess atmospheric absorption, *Geophys. Res. Lett.*, *25*, 3591–3594, 1998.

Hurrell, J. W., J. J. Hack, B. A. Boville, D. L. Williamson, and J. T. Kiehl, The dynamical simulation of the NCAR community

climate model version 3 (CCM3), *J. Clim.*, *11*, 1207–1236, 1998.

Jing, X., and R. D. Cess, Comparison of atmospheric clear-sky shortwave radiation models to collocated satellite and surface measurements in Canada, *J. Geophys. Res.*, *103*, 28793–28824, 1998.

Kato, S., T. P. Ackerman, E. E. Clothiaux, J. H. Mather, G. G. Mace, M. L. Wesely, F. Murcray, and J. Michalsky, Uncertainties in modeled and measured clear-sky surface shortwave irradiances, *J. Geophys. Res.*, *102*, 25881–25898, 1997.

Kiehl, J. T., and K. E. Trenberth, Earth's annual global mean energy budget, *Bull. Am. Meteorol. Soc.*, *78*, 197–208, 1997.

Kiehl, J. T., J. J. Hack, G. B. Bonan, B. A. Boville, D. L. Williamson, and P. J. Rasch, The National Center for Atmospheric Research Community Climate Model: CCM3, *J. Clim.*, *11*, 1131–1149, 1998a.

Kiehl, J. T., J. J. Hack, and J. W. Hurrell, The energy budget of the NCAR community climate model: CCM3, *J. Clim.*, *11*, 1151–1178, 1998b.

Michalsky, J., M. Beauharnois, J. Berndt, L. Harrison, P. Kiedron, and Q. Min, O_2-O_2 absorption band identification based on optical depth spectra of the visible and near-infrared, *Geophys. Res. Lett.*, *26*, 1581–1584, 1999.

Mlawer, E. J., S. A. Clough, P. D. Brown, T. M. Stephen, J. C. Landry, A. Goldman, and F. J. Murcray, Observed atmospheric collision-induced absorption in near-infrared oxygen bands, *J. Geophys. Res.*, *103*, 3859–3863, 1998.

Murcray, F. J., A. Goldman, J. C. Landry, and T. M. Stephen, O_2 continuum: A possible explanation for the discrepancies between measured and modeled shortwave surface irradiances, *Geophys. Res. Lett.*, *24*, 2315–2317, 1997.

Newnham, D. A., and J. Ballard, Visible absorption cross sections and integrated absorption intensities of molecular oxygen (O_2 and O_4), *J. Geophys. Res.*, *103*, 28801–28815, 1998.

Orlando, J. J., G. S. Tyndall, K. E. Nickerson, and J. G. Calvert, The temperature dependence of collision-induced absorption by oxygen near 6 μm, *J. Geophys. Res.*, *96*, 20755–20760, 1991.

Oshima, Y., Y. Okamoto, and S. Koda, Pressure effect of foreign gases on the Herzberg photoabsorption of Oxygen, *J. Phys. Chem.*, *99*, 11830–11833, 1995.

Osterkamp, H., F. Ferlemann, H. Harder, D. Perner, U. Platt, M. Schneider, and K. Pfeilsticker, First measurement of the atmospheric O_4 profile, in *Proceedings of the Fourth European Symposium on Polar Stratospheric Ozone*, edited by N. R. P. Harris, I. Kilbane-Dawe, and G. T. Amanatidis, *Air Pollut. Res. Rep. 66*, pp. 478–481, European Commission Environment and Climate Programme, Brussels, 1998.

Perner, D., and U. Platt, Absorption of light in the atmosphere by collision pairs of oxygen (O_2)$_2$, *Geophys. Res. Lett.*, *7*, 1053–1056, 1980.

Pfeilsticker, K., F. Erle, and U. Platt, Absorption of solar radiation by atmospheric O_4, *J. Atmos. Sci.*, *54*, 933–939, 1997.

Ramanathan, V., and A. M. Vogelmann, Greenhouse effect, atmospheric solar absorption and the Earth's radiation budget: From the Arrhenius-Langley era to the 1990s, *Ambio*, *26*, 38–46, 1997.

Shardanand, Nitrogen-induced absorption of Oxygen in the Herzberg continuum, *J. Quant. Spectrosc. Radiat. Transfer*, *18*, 525–530, 1977.

Shardanand, and A. D. P. Rao, Collision-induced absorption of O_2 in the Herzberg continuum, *J. Quant. Spectrosc. Radiat. Transfer*, *17*, 433–439, 1977.

Shine, K. P., R. G. Derwent, D. J. Wuebbles, and J.-J. Morcrette, Radiative forcing of climate, in *Climate Change: The IPCC Scientific Assessment*, edited by J. T. Houghton, G. J. Jenkins, and J. J. Ephraums, pp. 45–68, Cambridge Univ. Press, New York, 1990.

Solomon, S., R. W. Portmann, R. W. Sanders, and J. S. Daniel, Absorption of solar radiation by water vapor, oxygen, and related collision pairs in the Earth's atmosphere, *J. Geophys. Res.*, *103*, 3847–3858, 1998.

Stephens, G. L., and S.-C. Tsay, On the cloud absorption anomaly, *Q. J. R. Meteorol. Soc.*, *116*, 671–704, 1990.

Vogelmann, A. M., V. Ramanathan, W. C. Conant, and W. E. Hunter, Observational constraints on the non-lorentzian continuum effects in the near-infrared solar spectrum using ARM ARESE data, *J. Quant. Spectrosc. Radiat. Transfer*, *60*, 231–246, 1998.

Williamson, D. L., and J. G. Olson, A comparison of semi-Lagrangian and Eulerian polar climate simulations, *Mon. Weather Rev.*, *126*, 991–1000, 1998.

World Meteorological Organization, Atmospheric Ozone 1985, *Tech. Rep. 16*, Global Ozone Res. and Monitoring Proj., Geneva, 1985.

Zender, C. S., B. Bush, S. K. Pope, A. Bucholtz, W. D. Collins, J. T. Kiehl, F. P. J. Valero, and J. Vitko Jr., Atmospheric absorption during the Atmospheric Radiation Measurement (ARM) Enhanced Shortwave Experiment (ARESE), *J. Geophys. Res.*, *102*, 29901–29915, 1997.

C. S. Zender, Department of Earth System Science, University of California, Irvine, CA 92697-3100. (zender@uci.edu)